

Studies of the Structures of Nitrogen-Neon Nanoclusters Immersed into Superfluid Helium-4

C. K. Wetzel¹ · D. M. Lee¹ · V. V. Khmelenko¹

Received: 14 October 2023 / Accepted: 2 December 2023 / Published online: 17 January 2024 © The Author(s), under exclusive licence to Springer Science+Business Media, LLC, part of Springer Nature 2024

Abstract

We studied the electron spin resonance (ESR) spectra of nitrogen atoms stabilized in nitrogen-neon nanoclusters immersed in superfluid 4 He. The nanoclusters were formed during the condensation of the products of the discharge in N₂–Ne–He gas mixtures into bulk superfluid 4 He at temperature 1.5 K. We studied nanoclusters formed by injection of gas mixtures with different ratios of heavy impurities in the helium N₂/(Ne + N₂) ranging from 2% to 90%. Analysis of the ESR spectra of nitrogen atoms stabilized in nitrogen-neon nanoclusters provides important information about the environment of the stabilized atoms and a shell structure of the nanoclusters was revealed. For all samples studied, preferential stabilization of N atoms on the surfaces of the nanoclusters was observed. Annealing of the collection of the nanoclusters in the temperature range 1.1–10 K resulted in substantial changes in the structure of the nanoclusters.

Keywords Nanoclusters · Matrix isolation · Electron spin resonance

1 Introduction

Impurity-helium condensates (IHCs) consist of a collection of nanoclusters, which form a porous network immersed in superfluid helium-4 (HeII) [1–4]. Typical sizes of nanoclusters (3–10 nm) and the density of impurities in IHCs ($\sim 10^{20} cm^{-3}$) were determined from x-ray diffraction measurements [5–8]. The small densities of

C. K. Wetzel wetzecam@tamu.edu

> D. M. Lee dmlee@tamu.edu

V. V. Khmelenko khmel@tamu.edu

Institute of Quantum Science and Engineering, Department of Physics and Astronomy, Texas A&M University, College Station 77843, TX, USA



impurities result from the high porosity of IHCs. Ultrasound studies have shown a wide distribution of pore sizes in IHCs, ranging from 8 to 860 nm [3, 9–11]. IHCs form as a result of injecting mixtures of helium and impurity gases into bulk superfluid helium. When the mixture of gases first passes through a radio-frequency (RF) discharge zone before entering superfluid helium, a considerable concentration of free radicals can be stabilized in the nanoclusters forming IHCs [1, 12–16]. The stabilized atoms are then used as a probe to study their environment within the nanoclusters. Electron spin resonance is often used to study the effect of different environments on the stabilized atoms, and the structure of the nanoclusters [15–20]. Analysis of the ESR spectra of nitrogen atoms in nanoclusters formed by condensation nitrogen-rare gas-helium gas mixtures provided evidence for shell structure of nanoclusters [15, 16, 21, 22]. But the behavior of nitrogen atoms in different layers of nanoclusters during annealing has not yet been systematically studied. In this work, we used ESR to study the structures of nitrogen-neon-helium nanoclusters immersed in HeII. The nitrogen-neon-helium nanoclusters were formed in controllable conditions, by using a new design for the RF discharge. In contrast to previous work, the new design of the discharge cavity allows application of RF power comparable to the previous work (~ 50 W) to the discharge zone, without inducing substantial noise in the equipment controlling experimental conditions (temperature, pressure and level of liquid Helium). This has enabled us to use well reproducible conditions during the formation of collection of nanoclusters in IHCs. We performed studies of the structures of nanoclusters formed from nitrogen-neon-helium gas mixtures for a large range of N₂/Ne ratios. Our new results support the conclusion that nitrogen-neon nanoclusters which form IHCs have a shell structure, and observed preferential stabilization of N atoms on the surfaces of N_2 -Ne nanoclusters. Additionally, we investigated the changes in nanoclusters' structure caused by annealing the IHC samples. One of the goals of this work was to study the behavior of nitrogen atoms in different layers of nitrogen-neon nanoclusters during annealing in the temperature range 1.1-10 K. The effect of increasing of the local concentration of nitrogen atoms in neon layer during annealing was observed for the first time.

2 Experimental Setup

The experiments described in this paper were carried out in a Janis Research cryostat with a variable temperature insert (VTI) [22]. Figure 1 depicts the major systems external to the cryostat, whereas Fig. 2 details the components of the insert for the VTI. The VTI and 4K bath of the cryostat are insulated from one another by a vacuum jacket, while a capillary with a needle valve connects the two volumes, allowing for continuous filling of the VTI with liquid ⁴He during the experiment. Regulation of temperature within the VTI is achieved by a heater attached to the capillary, allowing control of the temperature of the He gas entering the volume. Cooling of the experiment was facilitated by pumping He gas from the VTI with a two stage pumping system consisting of an Edwards E2M80 vacuum pump along



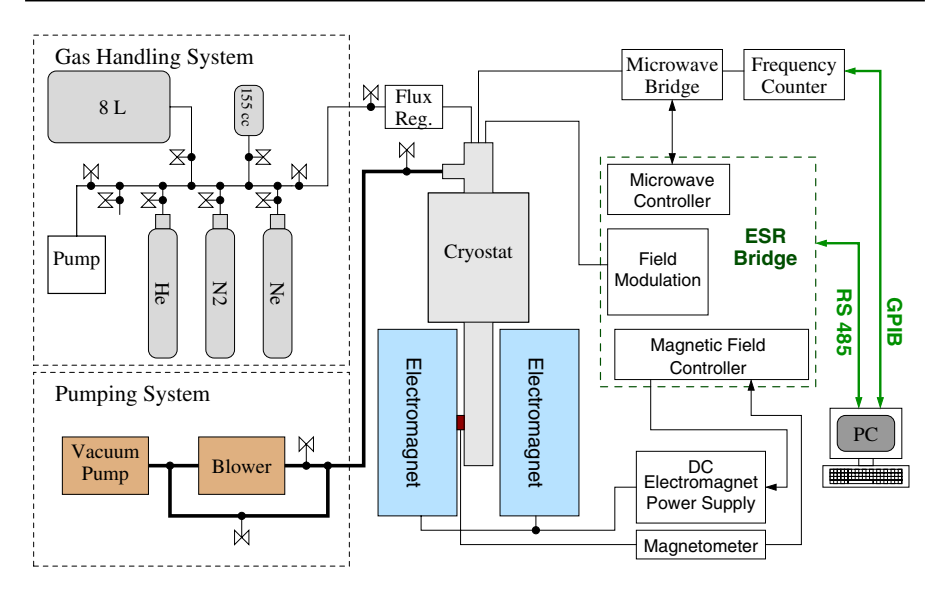


Fig. 1 Block diagram of the experimental setup

with a roots blower (booster) Edwards EH-1200. When utilizing the roots blower, VTI temperatures as low as 1.1K could be achieved.

The gas mixtures, used to form the IHC samples, were first prepared in the gas handling system (see Fig. 1) before being introduced through a quartz capillary to the VTI. The gas handling system consisted of two auxiliary volumes (8 L and 155 mL), an Edwards E2M-18 vacuum pump, pressurized cylinders containing the gases to be mixed, an analog pressure gauge, and plumbing connecting to the cryostat through a Brooks 5850E flux regulator. All components interconnect through a central manifold, and all plumbing of the manifold was constructed from copper piping and cylinders. Linde Research purity 4 He gas, Matheson Research purity 4 He gas, Matheson Research purity N₂ gas, and Matheson Research purity Ne were used, without additional purification, to prepare the gas mixtures which were used to form the IHC samples.

A commercial Bruker EMX PLUS spectrometer, along with a Varian 7800 electromagnet (capable of producing fields up to 1 T) and a homemade X-band ($f_0 \approx 8.91$ GHz) resonant cavity [22, 23] were used to facilitate homodyne registration of the ESR spectra of stabilized atoms measured in these experiments. The precision of magnetic field measurement is 10^{-6} T. The ESR cavity (located within the VTI volume) was centered within the homogenous field region of the Varian magnet, which provided a constant background field. The Bruker ESR console produced a modulating magnetic field of 0.5 G peak-peak amplitude and 100 kHz frequency. An EIP 545B microwave frequency counter was used to record the klystron frequency during the ESR registrations.

The experimental measurements were taken within the innermost volume of the cryostat, containing the VTI (Fig. 2). The main components of the low-temperature insert for the VTI include the quartz tube system, a movable quartz beaker, a fountain pump, and the ESR microwave cavity.



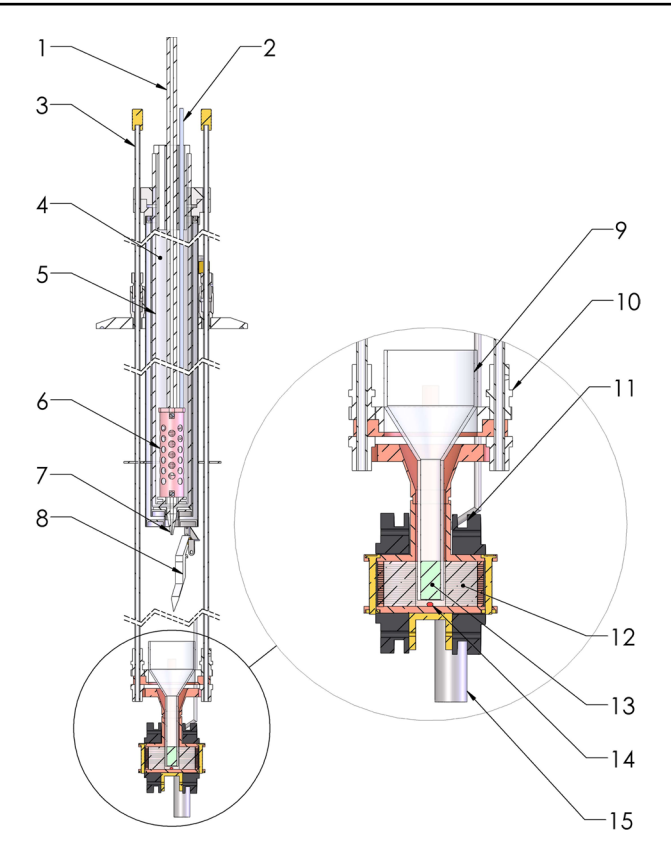


Fig. 2 Low-temperature insert for the VTI used in these experiments. 1-quartz capillary, 2-coaxial cable to RF discharge cavity, 3-tubes for vertical displacement and rotation of the beaker, 4-liquid nitrogen bath, 5-quartz tube, 6-RF discharge cavity, 7-orifice of quartz capillary, 8-teflon blades, 9-quartz beaker, 10-teflon gear for beaker rotation, 11-modulation coil, 12-quartz cylinder, 13-IHC sample, 14-ruby crystal, 15-fountain pump

The quartz tube (see Fig. 2) is the first stage experienced by the prepared gas mixture as it enters the cryostat. The quartz tube consists of an outer tube connected to a quartz capillary running down the center, and houses the discharge cavity which produces free radicals. The quartz tubing is filled with liquid nitrogen, which acts both to precool the gas mixture, and provide cooling power to the discharge cavity independent from the main ⁴He cooling power of the VTI. The quartz tube resides in a metallic vacuum jacket, which provides insulation from the cold He gas and allows the nitrogen in the outer quartz tube to remain in the liquid phase.

2.1 Sample Preparation

For sample preparation, the quartz beaker was moved upward within the VTI until it reached the top position (~ 2 cm under the orifice of the quartz capillary). The fountain pump was then utilized to fill the beaker with superfluid ⁴He. After waiting



sufficient time (\sim 10–15 s) for the beaker to fill and the VTI temperature to stabilize at $T \approx 1.4$ K, pure 4 He gas was fed through the quartz capillary, and the discharge was ignited [24, 25]. By first applying the discharge to pure 4 He, the possibility of the impurity gases freezing near the orifice of the cold capillary was eliminated, and the VTI conditions were allowed to stabilize at $T \approx 1.5$ K with the added heat load from the flux of gas and the discharge. Once the discharge was ignited and conditions stabilized, the as-prepared nitrogen-neon-helium gas mixture replaced the pure helium gas and the IHC formation process proceeded. This process ran for a period of about 8 min, with the beaker intermittently rotated in order to collect more of the sample in the cylindrical region of the beaker (see Fig. 2). After this period, the beaker with accumulated sample was promptly (\leq 5 min before first ESR registration) lowered into the ESR microwave cavity for study (see Fig. 2).

2.2 RF Discharge Cavity

A long-standing issue, which plagued previous experiments of this nature, was strong radio-frequency (RF) emissions of the discharge source which interfered with many laboratory devices both inside and outside the cryostat alike. This stray coupling was manifested as errors picked up in unrelated digital electronics and strong interference with sensitive analog devices, e.g., thermometry lock-in amplifiers. The previous design consisted of two independent coaxial cables terminated by capacitively coupled electrodes [4, 24], and required turning off all measurement equipment during sample accumulation.

Our goal was to design a new discharge cavity, in order to reduce the radiation losses by utilizing a single coaxial cable to drive the cavity, as well as shielding the high voltage electrodes from the rest of the cryostat. After a series of prototypes,

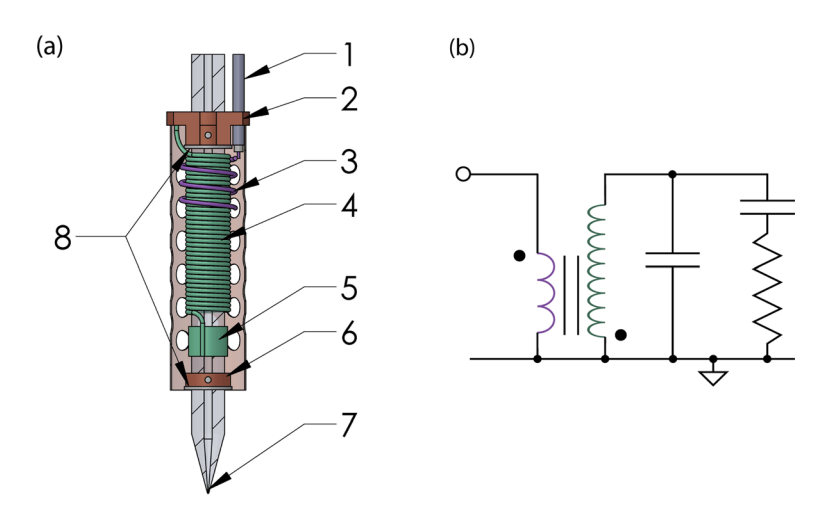


Fig. 3 Discharge cavity. **a** Cross-section view of discharge cavity. 1-coaxial transmission line, 2-top cap, 3-primary coil, 4-secondary coil, 5-electrode, 6-bottom cap, 7-quartz capillary orifice, 8-teflon spacers. **b** Overtly idealized equivalent circuit of the discharge cavity



the design converged to that depicted in Fig. 3. Although the new design still suffers from measurable RF radiation, the undesired effects of RF pickup on other equipment was negligible.

2.2.1 Construction

The discharge element was constructed from a variety of generic materials found in the laboratory. The body (shielding) of the discharge cavity was machined from a 5/8" copper pipe (O.D. = 0.625", I.D. = 0.55"). In order to combat the issue of overheating, the thermal mass of the body was reduced by turning down the diameter of the pipe on a lathe. The final O.D. of the body was 0.57" (\approx 14.5 mm), resulting in a wall thickness of 0.02" (\approx 0.5 mm). After reducing the diameter, perforation was added to the body by drilling a cylindrically symmetric hexagonal lattice hole pattern with a #24 Drill (diameter = 0.152" \approx 3.9 mm). The perforations served to improve the efficiency of cooling by improving the ability of liquid N₂ to penetrate the cavity.

The primary and secondary coils were hand wound from 20 AWG copper magnet wire. The secondary coil consists of 32 turns, originally wound around a 0.25" (\approx 6.35 mm) steel rod. The final length of the secondary coil was 1.1" (\approx 2.8 cm). The primary coil was formed by winding 3 turns (in the same direction as the secondary) around a steel rod of diameter 0.8" (\approx 9.7 mm) over a length of 0.75" (\approx 9.5 mm). The diameter of the primary coil was made larger than the secondary in order to provide space between the coils, as dielectric breakdown of the wire enamel was observed when the coils were in physical contact with one another.

The electrode was made by wrapping a copper strip of thickness 0.015" (≈ 0.381 mm) and width 0.225" (≈ 5.7 mm) around the same rod used to wind the secondary coil. The electrode was then attached to the secondary coil, by soldering an exposed length of the secondary wire along the side of the electrode.

The most complex parts of the discharge assembly, the top and bottom caps, were designed to maximize the admittance of liquid N_2 into the cavity, and machined from standard copper. For ease of disassembly the top and bottom caps attached to the cavity body via bolts (rather than solder), forming a pressure electrical contact. In order to ensure reliable electrical contact at cryogenic temperatures, brass bolts were used to secure the copper pieces so that the connection would tighten with decreased temperature. Additionally, thin TeflonTM (PTFE) spacers were made to fit between copper caps and the quartz capillary. These spacers served to prevent the possibility of a glass-metal contact at cryogenic temperature which could potentially damage the capillary.

2.2.2 Operation

The discharge cavity operates as a capacitively coupled plasma (CCP) device. By inducing a voltage difference between the electrode and the cavity body, a strong electric field, with nonzero component along the capillary axis, forms and facilitates plasma production within the quartz capillary. A solenoid (the secondary coil) in series with the electrode forms an LC tank circuit (see Fig. 3b), which resonates at frequency ~90MHz



in air at STP, and at ~75MHz when immersed in liquid nitrogen. This resonance may also be viewed as an impedance match, bringing the impedance of the capacitor/plasma closer to the 50 Ω impedance of the coax. Rather than driving the system directly from the coax, a shorter coaxial solenoid (primary coil) inductively couples to the secondary coil. The pair of solenoids form a step-up transformer with turn ratio ~ 10 . However, due to non-ideal coil placement the voltage gain can be degraded significantly. The transformer configuration also serves as a method for further impedance matching by reducing the impedance seen by the amplifier. A Stanford Research System Model SG386 signal generator and an E &I 4100 L RF amplifier, with nominal voltage gain of 60dB and a bandwidth of 150 MHz, was used to drive the plasma cavity. The amplifier includes a built in reflectometer at its output, allowing us to monitor the applied and reflected power at the output of the amplifier. We found that applying 75 MHz at ≈ 14 W (of which ≈ 7 W were reflected back) was sufficient to produce IHC samples, with stabilized N atoms, similar to the previous design, without overheating.

3 Experimental Results

3.1 Stabilization Efficiency

We studied the dependence of N atom stabilization efficiency in N₂-Ne-He condensates, by varying the ratio of the impurity gases [N₂]:[Ne] in the initial gas mixture. For small ratio of [N₂]:[Ne] the ratio of the impurity gases to He was fixed at 1/50, whereas at higher N₂ content (i.e., [N₂]/[Ne] > 1) the He content was increased to 1/100, in order to reduce the possibility of impurity gas freezing in the capillary due to the relatively high melting point of N₂ ($T_{melt} \approx 63K$). The ESR spectra of N atoms stabilized in nitrogen-neon nanoclusters prepared from different nitrogen-neon-helium gas mixtures are shown in Fig. 4.

The total number of N atoms stabilized in each sample was calculated by taking the double integral of the N atom ESR signals, and comparing them to the double integral of the Ruby reference signals taken under similar conditions [15, 16]. Knowing the volume of the sample within the ESR cavity and the sensitivity characteristics of the cavity to the sample within this volume, the average concentration (N_{avg}) of N atoms in the sample was calculated using the following equation,

$$N_{avg} = \left(N_R \cdot \frac{I_N}{I_R} \cdot \gamma \cdot \frac{4}{3}S(S+1)\right) / V_s \tag{1}$$

where $N_R = 6.417 \cdot 10^{16}$ is the number of spins in the reference ruby crystal, $\gamma = 2.66$ is the sensitivity correction factor for the non-uniform sensitivity of the cavity [14], $S = \frac{3}{2}$ is the electron spin of a N^{14} atom, $V_s = 0.352$ cm³ is the volume of the sample within the ESR cavity, and I_N , I_R are the doubly integrated Nitrogen and Ruby ESR signals, respectively. The results of these calculations for a variety of impurity gas ratios, expressed as percentage of N_2 in the N_2 -Ne mixture, are presented in Fig. 5. The efficiency of stabilization (κ) for nitrogen atoms in the sample was calculated as the ratio of the total number of stabilized atoms (N_{tot}), to the number of atoms sent



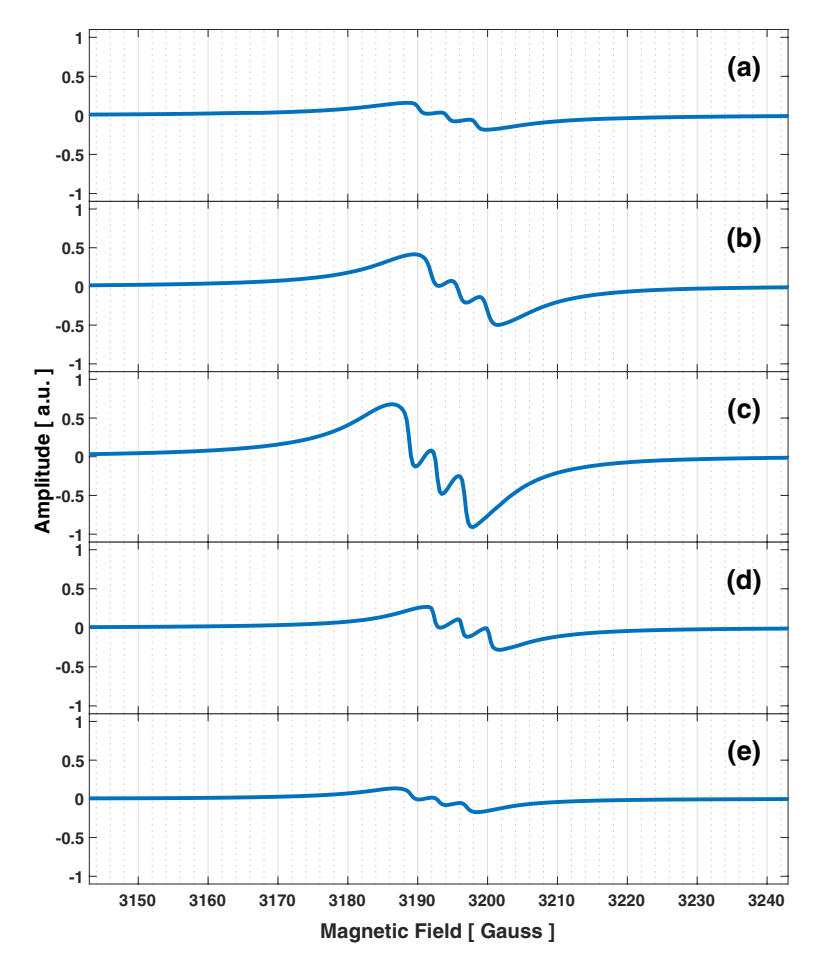


Fig. 4 ESR spectra of N atoms stabilized in samples prepared from a variety of nitrogen-neon-helium gas mixtures: **a** [N₂]:[Ne]:[He] = 8:1:900, **b** [N₂]:[Ne]:[He] = 2:1:300, **c** [N₂]:[Ne]:[He] = 1:2:150, **d** [N₂]:[Ne]:[He] = 1:10:550, **e** [N₂]:[Ne]:[He] = 1:50:2550

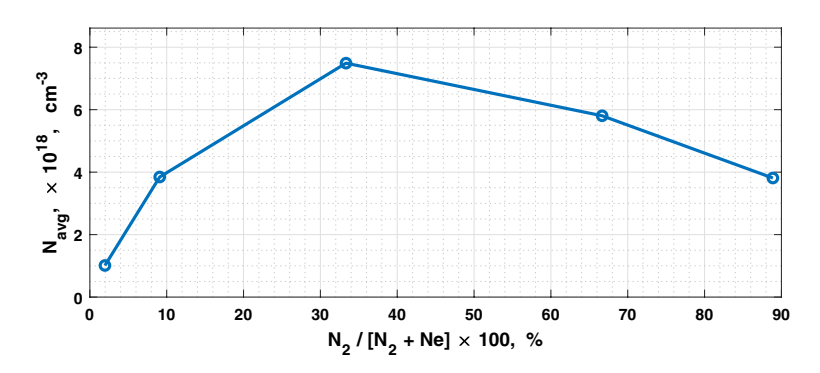


Fig. 5 Dependence of the average concentration of N atoms stabilized in the N_2 -Ne-He samples, on ratio of N_2 /(Ne + N_2) (%) in the condensed gas mixtures



from the discharge into the helium filled beaker (N_i) . The following formula was used:

$$\kappa = \frac{N_{tot}}{N_i} = \left(N_{avg} \cdot V_s\right) / \left(\frac{dN_2}{dt} \cdot t \cdot \sigma \cdot 2\right)$$
 (2)

where t = 480 s (8 min) is the time of sample accumulation, and $\sigma = 30\%$ is the efficiency of dissociation for N₂ for the RF discharge cavity. The results of applying Eqs. (1) and (2) to the first measurements taken just after the accumulation process, as well as the conditions of sample preparation are presented in Table 1.

3.2 Structure of Nanoclusters

Information regarding the surroundings of the stabilized nitrogen atoms within the nanoclusters was extracted by analyzing the line shape of the ESR signals. From previous work [15, 16], it is known that the nanoclusters which compose the IHC samples possess a shell structure, as depicted in Fig. 6. In order to extract information on the nanoclusters' structure, each nitrogen ESR spectra was fit as the superposition of three independent Lorentzian derivative triplets (see Fig. 7) of known hyperfine constants. We identify the triplet (red line) in Fig. 7b with N atoms stabilized in the Ne matrix (A= 4.10 G); the broader triplet (yellow line) in Fig. 7b is assigned to N atoms stabilized in N_2 matrix (A = 4.20 G); and the singlet (blue line) in Fig. 7b belongs to N atoms residing on the surfaces of the nanoclusters (see Table 2).

The line widths and amplitudes of the fit spectra components allow interpretation of the local concentration of *N* atoms and the relative weights of each of the comprising spectra. Spectral broadening can be attributed to dipole-dipole interactions between N atoms in the sample. The following equation relates the observed line width to the local concentration of stabilized atoms [30]:

$$\Delta H_{pp} = 2.3g\mu_0 \sqrt{S(S+1)} n_{\text{local}}$$
 (3)

where ΔH_{pp} is the peak-to-peak line-width of the ESR line in Gauss, g is the electron g-factor, μ_0 is the Bohr magneton, S is the overall electron spin (S=3/2 for 14 N atom), and n_{loc} the local concentration of nitrogen atoms with units atoms \cdot cm^{-3} .

Table 1 Flux of nitrogen-neon-helium mixtures used for preparation of IHCs, average concentrations of $N(^4S)$ atoms within IHCs, and N atom stabilization efficiency

Gas mixture [N ₂]:[Ne]:[He]	Flow rate $\frac{dN_2}{dt}$, s ⁻¹	Average concentration N_{avg} , cm^{-3}	N atom stabilization Efficiency, κ , %	
1:50:2550	1.92×10^{16}	1.01×10^{18}	6.44	
1:10:550	8.91×10^{16}	3.84×10^{18}	5.27	
1:2:150	3.27×10^{17}	7.49×10^{18}	2.80	
2:1:150	6.54×10^{17}	5.80×10^{18}	1.09	
8:1:900	4.40×10^{17}	3.81×10^{18}	1.06	



Table 2 Hyperfine splitting constants, *A*, and *g* factors of nitrogen atoms stabilized in different matrices and in nitrogen-neon-helium condensates

Matrix	A, G	g factor
Free [26]	3.73	2.00215
N ₂ [27]	4.20	2.00216
Ne [28]	4.10	2.0017
Ne [29]	4.02	2.00195
N ₂ :Ne:He - Surface [16, 19]	4.12	2.00232
N ₂ :Ne:He - Neon [16, 19]	4.10	2.00223
N ₂ :Ne:He–N ₂ [16, 19]	4.20	2.00215

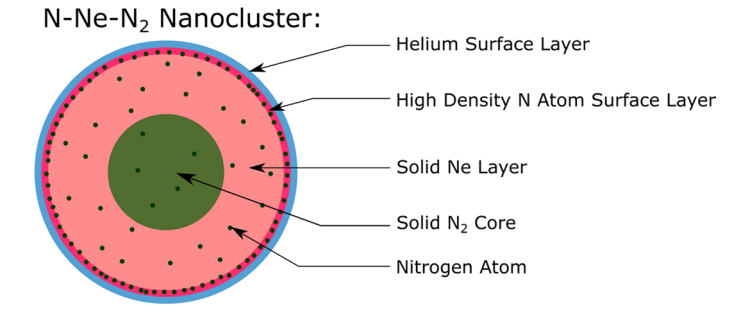


Fig. 6 Diagram depiction of the shell structure of the N₂-Ne nanoclusters with stabilized nitrogen atoms

The MATLAB Curve Fitter application was used to facilitate the fitting of our model to each of the recorded spectra. Figure 8 presents the behavior of the local concentration of nitrogen atoms for each shell, as the content of the gas mixture was varied. Table 3 presents the same data, with the addition of the weight of each shell contributing to the overall signal as well as the observed g factors.

3.3 Annealing of N-N₂-Ne Nanoclusters

We also studied the influence of warming the sample on the structure of N_2 -Ne nanoclusters and on the average and local concentrations of stabilized N atoms in the sample. This was accomplished by incrementally increasing the temperature over the range 1.1–10 K, recording the ESR spectra of the nitrogen atoms and ruby at each temperature. Figure 9 presents the evolution of the ESR spectrum of a selected sample as the temperature was increased. Applying Eq. (1) we calculated the average concentration of N atoms at different temperatures. Figure 10 presents the dependence of the average concentration of nitrogen atoms on temperature for three different samples. For samples with sufficiently high initial nitrogen atom concentration, there exists a maximum in average concentration, $N_{avg} = 2.5 \times 10^{19}$, around $T \approx 3K$. During heating from 1.1 K to 3.0 K, we observed an increase in the intensity of the N atom ESR signal (see Fig 9a and b). The increase in the N atom ESR signal at T = 3.0 K is due to the collapse of



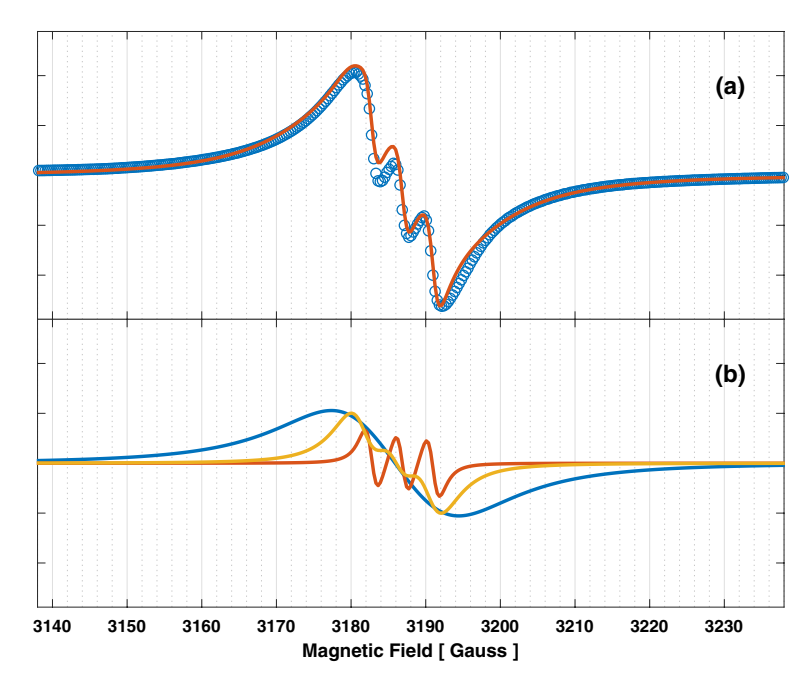


Fig. 7 ESR spectrum of N atoms for nitrogen-neon-helium sample formed from $[N_2]$:[Ne]:[He] = 1:50:2550 gas mixture. **a** The experimental data (blue circles), the fit sum of three Lorentzian triplet spectra (solid red line). **b** The three fitting Lorentzian triplets independently, corresponding to the three different environments of N atoms: N atoms on the surfaces (blue), N atoms in Ne matrix (red) and N atoms in N_2 matrix (yellow)

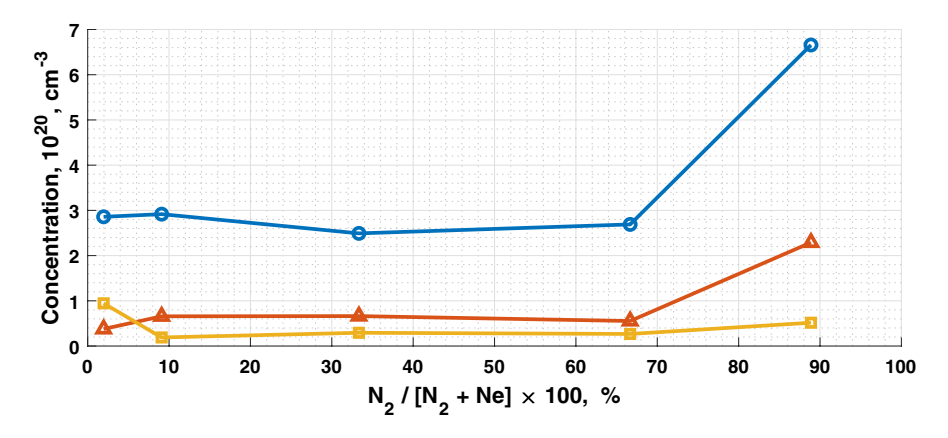


Fig. 8 Dependence of local concentration of N atoms in N_2 -Ne nanoclusters, stabilized on nanocluster surfaces (blue circles), in Ne matrix (red triangles) and in N_2 matrix (yellow squares), on the ratio of N_2 / (Ne + N_2) in the gas mixture used for sample preparation



Table 3 Results from analysis of ESR spectra of N atoms stabilized in nitrogen-neon nanoclusters, pre-
pared from different N2:Ne:He gas mixtures. Here, A is the hyperfine structure constant, g factors of the
N atoms, and ΔH_{pp} the peak-to-peak linewidth for the ESR spectra

Gas mixture	A, G	ΔH_{pp} , G	n_{loc}, cm^{-3}	Weight, %	g factor ^a
$[N_2]:[Ne]:[He] = 1:50:2550$	4.12	13.75	2.86×10^{20}	83.29	2.0028
	4.1	1.81	3.77×10^{19}	2.14	2.0022
	4.2	4.54	9.44×10^{19}	14.57	2.0027
$[N_2]$: $[Ne]$: $[He] = 1:10:550$	4.12	14.03	2.92×10^{20}	88.46	2.0023
	4.1	3.16	6.57×10^{19}	11.11	2.0021
	4.2	0.91	1.90×10^{19}	0.43	2.0022
$[N_2]$: $[Ne]$: $[He] = 1:2:150$	4.12	11.99	2.49×10^{20}	93.30	2.0028
	4.1	3.19	6.62×10^{19}	5.38	2.0026
	4.2	1.41	2.94×10^{19}	1.31	2.0023
$[N_2]$: $[Ne]$: $[He] = 2:1:150$	4.12	12.94	2.69×10^{20}	93.26	2.0030
	4.1	2.66	5.54×10^{19}	6.61	2.0022
	4.2	1.28	2.67×10^{19}	0.13	2.0035
$[N_2]$: $[Ne]$: $[He] = 8:1:900$	4.12	32.03	6.66×10^{20}	55.93	2.0028
	4.1	9.54	2.29×10^{20}	41.30	2.0026
	4.2	2.48	5.16×10^{19}	2.77	2.0022

The g factor was calculated from the center field H_0 , units G, of the respective triplet and the applied microwave frequency v, units MHz, using the equation $hv = g\mu_0H_0$

the pores in the sample, which results in an increase in the sample density, which allows an additional sample to enter the sensitive region of the ESR cavity. This additional part of the sample was initially accumulated in the beaker above the ESR cavity. Further heating to $T=4.0~\rm K$ led to the recombination of the majority of N atoms, leaving only a small well resolved signal from the remaining N atoms (see Fig. 9c).

Additionally, we studied the behavior of atoms stabilized in different environments corresponding to the three different shells of the nanoclusters as the sample was warmed through the temperature range of 1.1–10 K. In order to obtain information on the structure of the nanoclusters, we used the same approach of representing the experimental spectra at different temperatures as a sum of three Lorentzian triplets corresponding to N atoms on the surfaces of nanoclusters, N atoms in Ne matrix, and N atoms in N_2 matrix, respectively. From this analysis, we obtained the linewidths and integrals of each fitted Lorentzian. Variations in local concentration of N atoms, which correspond to changes in the linewidths, resulting from increasing temperature are presented in Fig 11. From the integrals of the fitted Lorentzians, we calculated the dependence of the total number of N atoms in each layer of the nanoclusters, as the temperature increased. This temperature dependence is shown in Fig. 12. From Fig. 12, one can see that the majority of N atoms which recombined initially resided on the surfaces, while the N atoms initially stabilized in the Ne and N_2 layers mostly survived.



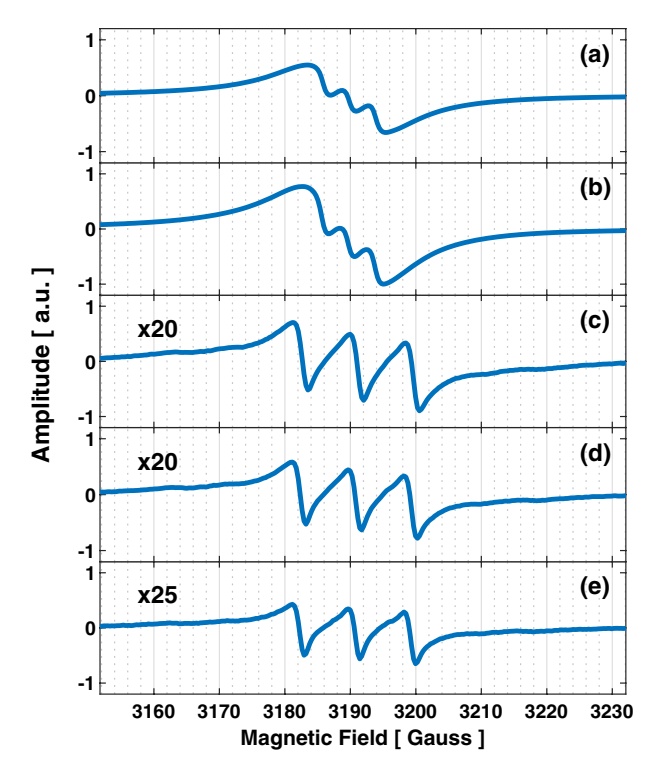


Fig. 9 ESR Spectra of N atoms stabilized in sample prepared from the gas mixture $[N_2]$: $[N_2]$: $[H_2]$ = 2:1:150. Starting immediately after accumulation at T = 1.3K (a) and after annealing at temperatures 3K (b), 4K (c), 5K (d), and 10K (e)

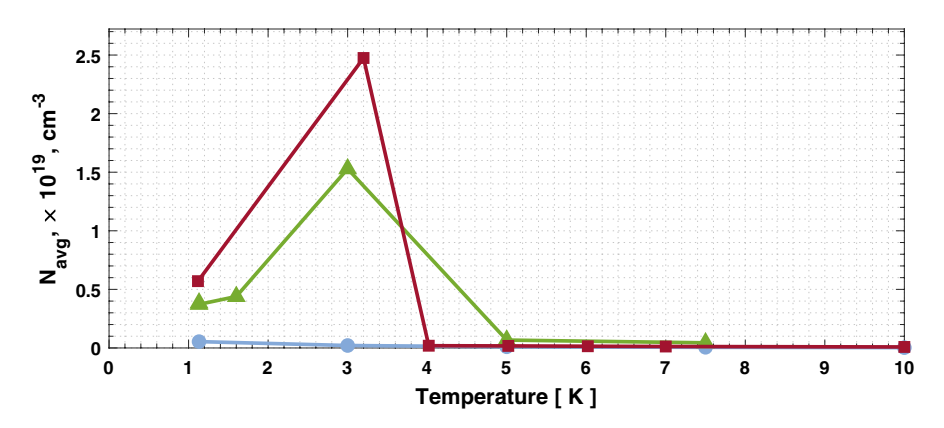


Fig. 10 Dependence of the average concentration of N atoms on temperature for samples prepared from different gas mixtures: $[N_2]$:[Ne]:[He] = 1:20:1050 (blue circles); $[N_2]$:[Ne]:[He] = 1:10:550 (green triangles); $[N_2]$:[Ne]:[He] = 2:1:150 (red squares)



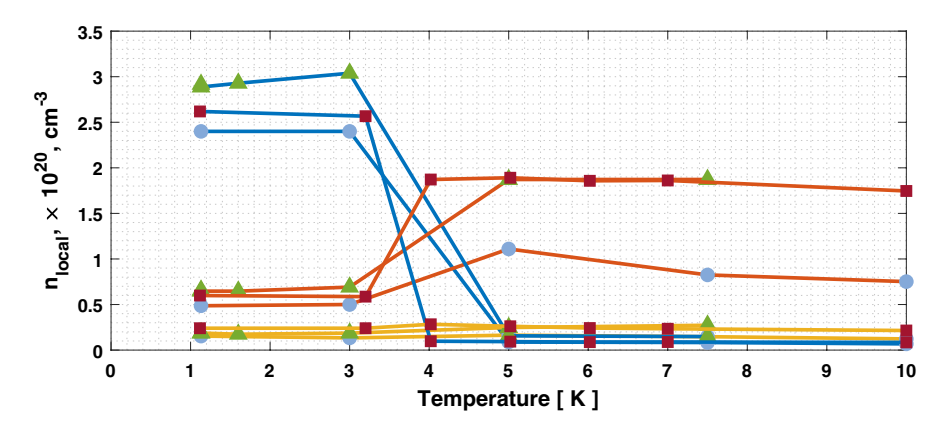


Fig. 11 Dependence on temperature of local concentration of N atoms stabilized on the surfaces of nanoclusters (blue lines), in Ne matrix (red lines) and in N_2 matrix (yellow lines) for samples prepared from different gas mixtures: $[N_2]$:[Ne]:[He] = 1:20:1050 (blue circles); $[N_2]$:[Ne]:[He] = 1:10:550 (green triangles); $[N_2]$:[Ne]:[He] = 2:1:150 (red squares)

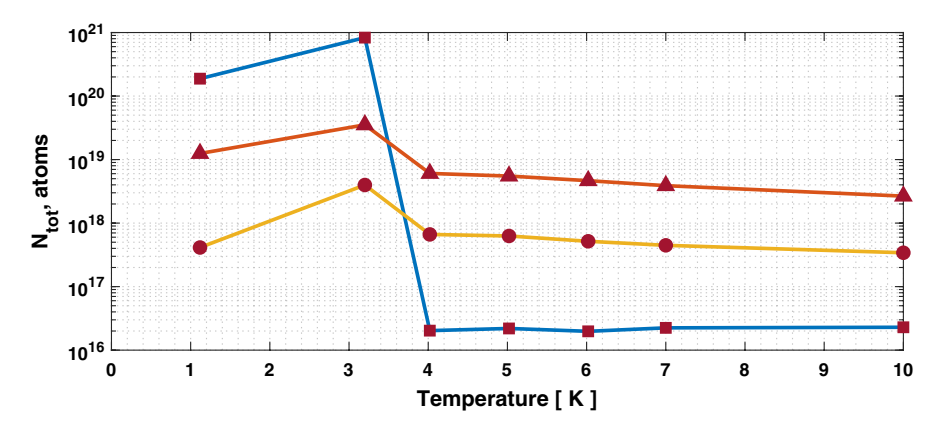


Fig. 12 Dependence on temperature of total number of N atoms stabilized on the surfaces of nanoclusters (squares; blue line), in Ne matrix (triangles; red line) and in N_2 matrix (circles; yellow line) for the sample prepared from the gas mixture $[N_2]$: $[N_2$

4 Discussion

Impurity-helium condensates (IHC) are a class of non-crystalline nanomaterials, which hold the record, among all materials, for the largest local concentration of stabilized atoms [1, 2, 14–16]. The method of forming IHCs is based on injection of the products of a gas discharge into bulk HeII. The previous design of discharge characterized by high atomic stabilization efficiency, has the deficiency of emitting strong RF noise which interfered with both measurement and control equipment of the experiments [4, 24, 25]. This deficiency does not permit systematic studies of the optimal conditions for stabilizing atoms in IHCs. The task of designing and realizing an RF discharge cavity for efficient production and stabilization of free atoms



in IHCs is very important. We designed and built a new discharge cavity, for efficient stabilization of atoms in IHCs, without producing substantial RF noise effecting measurement equipment.

The new design of the discharge cavity was used in the present work, for studying nitrogen-neon-helium condensates containing stabilized nitrogen atoms. The new discharge cavity provides better reproducibility of the conditions for IHC sample preparation. In the present work, we studied the efficiency of stabilization of N atoms and the structure of nitrogen-neon-helium nanoclusters in IHCs prepared from gas mixtures with different N₂/Ne ratios. It was found that the average concentration of N atoms in different nitrogen-neon-helium condensates prepared by using the new discharge design is close to that of similar IHCs prepared by using the old discharge design [16]. In Fig. 13, the results for measurements of the average concentration of N atoms in N₂-Ne-He condensates, prepared by using both (new and old) designs of the discharge are superimposed. Further comparison of the data on nanocluster structure and local concentrations of N atoms (Table 3) with the previous results [16], suggests that the new discharge cavity design produced samples which were similar both in structure and quantity of stabilized atoms, to those produced from the old design.

When comparing the stabilization efficiency of the N atoms in the resulting IHCs (shown in Table 1), it may appear that the efficiencies stated in this work were notably higher than those presented previously [16]. However, this apparent discrepancy in results can likely be attributed to the much larger helium content in the gas mixtures used in this work, as studies on IHCs formed from pure nitrogen-helium mixtures showed a tendency of increasing stabilization efficiency as the helium content increased [16].

New studies of nitrogen-neon-helium condensates also support the shell structure model of N_2 -Ne nanoclusters forming condensates. The observed shell structure was similar for all samples prepared from gas mixtures with different N_2 /Ne ratios. Most of the N atoms stabilized on the outer surface shell, much fewer N

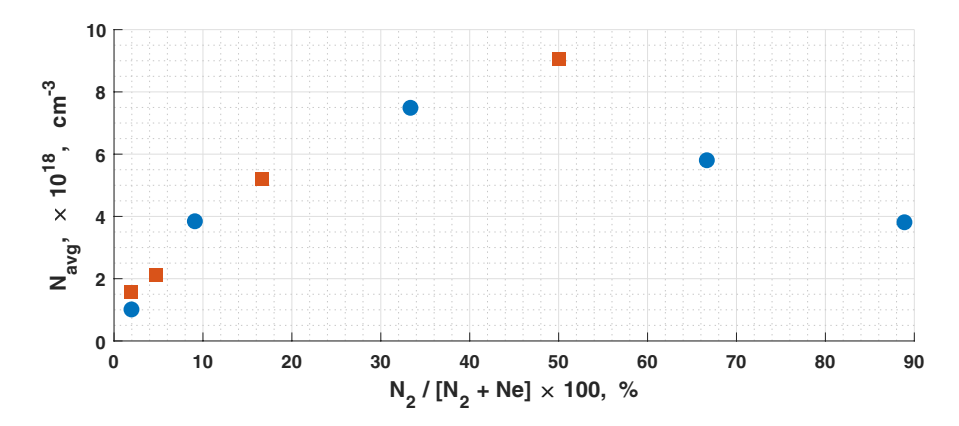


Fig. 13 Dependence of average concentration of N atoms stabilized in nitrogen-neon-helium condensates, on ratio $N_2/(Ne + N_2)$ in gas mixtures used for preparation of IHCs (blue circles) data presented in Table 1, and (red squares) data published previously [16]



atoms stabilized in the intermediate Ne shell, and substantially less stabilized in the N_2 core (see Fig. 6). The structure was determined by van der waals interactions between the atoms and molecules which compose the nanoclusters [16, 31].

The annealing of nitrogen-neon-helium condensates in the temperature range 1.1-3 K caused compression of the porous sample, which led to an increase in the average concentration of stabilized N atoms in the samples. Further heating from 3 K to 5 K lead to destruction of the outer layer containing the majority of stabilized N atoms, but the number of N atoms stabilized in the Ne and N_2 layers was almost preserved (see Fig. 12). Moreover, the local concentrations of N atoms in the intermediate Ne layer increased (see Fig. 11), showing effective diffusion of N atoms into the Ne layer. Even further heating from 5 to 10 K did not change the structure of the nanoclusters or the concentrations of stabilized nitrogen atoms.

It is known from previous studies, involving electron diffraction[32] and atomic nitrogen 2 D- 4 S emissions [33] on nitrogen-neon binary solids formed by cold vapor deposition, that these samples do not crystallize but rather form amorphous solids. Only at the ratio of $[N_2]$:[Ne] = 1:1 did the condensed mixtures show any signs of forming a face-centered cubic crystalline phase [32]. The preliminary data presented in Fig. 13 ostensibly suggests a maximum in average concentration of N atoms in the IHC samples formed from gas mixture with the ratio $[N_2]$:[Ne] = 1:1. This apparent maximum in average concentration seems to coincide with the nitrogen-neon gas mixture which showed evidence of a crystalline structure when condensed by cold vapor deposition.

With the benefit of eliminating the RF interference with sensitive equipment, it is now possible to operate and control the entire experiment while the discharge operates, including the ESR spectrometer. In future experiments, we intend to eliminate the movement of the beaker for the sample preparation process, by placing the discharge closer to the ESR cavity in order to form IHCs directly inside the cavity. If successful this new apparatus will enable us to study the formation process of IHCs composed of any gas mixture, i.e., not limited to IHCs containing nitrogen.

5 Conclusion

- The new design for discharge was used for preparation of nitrogen-neon-helium 4 condensates with high concentration of stabilized nitrogen atoms. This design allows formation of condensates without interrupting the performance of surrounding equipment.
- 2. The structures of nitrogen-neon-helium condensates were studied by ESR spectroscopy. The IHCs were prepared by using a broad range of N₂/Ne ratios in condensed N₂-Ne-He gas mixtures. The obtained results support earlier conclusions [15, 16] that nitrogen-neon nanoclusters which form IHCs have a shell structure. Most of the N atoms stabilized on the surfaces of nanoclusters, less N atoms stabilized in the Ne layer and even fewer N atoms stabilized in the N₂ core of the nanoclusters. This shell structure was the same for all IHCs prepared from gas mixtures with different N₂/Ne ratios.



3. Behavior of the nitrogen atoms in different layers of nitrogen-neon nanoclusters were studied as the sample warmed from 1.1 to 10 K. Warming of the samples from 1.1 K to 3 K led to increasing of the average concentration of N atoms in the sample due to collapsing pores and increasing sample density. The local concentration of nitrogen atoms in different layers did not change in this temperature range. Explosive destruction of the samples was observed in the temperature range 3–5 K for samples of different initial concentrations of nitrogen atoms. During destruction most of the nitrogen atoms on the surfaces recombined. ESR lines from nitrogen atoms on the surfaces nearly disappeared, but the local concentration of nitrogen atoms stabilized in the Ne layer increased due to diffusion of N atoms. The local concentration of nitrogen atoms in the N₂ core of nitrogen-neon nanoclusters does not change substantially during annealing in this temperature range.

Acknowledgements The authors greatly acknowledge the support by the National Science Foundation Grant No. DMR 2104756. CKW acknowledges the support of the HEEP fellowship.

References

- E.B. Gordon, V.V. Khmelenko, A.E. Popov, A.A. Pelmenev, O.F. Pugachev, Chem. Phys. Lett. 155, 301 (1989)
- E.B. Gordon, V.V. Khmelenko, A.A. Pelmenev, E.A. Popov, O.F. Pugachev, A.F. Shestakov, Chem. Phys. 170, 411 (1993)
- 3. S.I. Kiselev, V.V. Khmelenko, D.M. Lee, Low Temp. Phys. 26, 641 (2000)
- 4. V.V. Khmelenko, H. Kunttu, D.M. Lee, J. Low Temp. Phys. 148, 1 (2007)
- V. Kiryukhin, B. Keimer, R.E. Boltnev, V.V. Khmelenko, E.B. Gordon, Phys. Rev. Lett. 79, 1774 (1997)
- S.I. Kiselev, V.V. Khmelenko, D.M. Lee, V. Kiryukhin, R.E. Boltnev, E.B. Gordon, B. Keimer, Phys. Rev. B 65, 024517 (2002)
- V. Kiryukhin, E.P. Bernard, V.V. Khmelenko, R.E. Boltnev, N.V. Krainyukova, D.M. Lee, Phys. Rev. Lett. 98, 195506 (2007)
- 8. N.V. Krainyukova, R.E. Boltnev, E.P. Bernard, V.V. Khmelenko, D.M. Lee, V. Kiryukhin, Phys. Rev. Lett. 109, 245505 (2012)
- S.I. Kiselev, V.V. Khmelenko, D.A. Geller, D.M. Lee, J.R. Beamish, J. Low Temp. Phys. 119, 357 (2000)
- 10. S.I. Kiselev, V.V. Khmelenko, D.A. Geller, J.R. Beamish, D.M. Lee, Physica B 284, 105 (2000)
- 11. S.I. Kiselev, V.V. Khmelenko, D.M. Lee, J. Low Temp. Phys. 121, 671 (2000)
- E.B. Gordon, A.A. Pelmenev, O.F. Pugachev, V.L. Tal'roze, V.V. Khmelenko, Doklady Phys. Chem. 280(4–6), 145 (1985)
- 13. E.P. Bernard, R.E. Boltnev, V.V. Khmelenko, D.M. Lee, J. Low Temp. Phys. 134, 199 (2004)
- R.E. Boltnev, I.N. Krushinskaya, A.A. Pelmenev, E.A. Popov, D.Yu. Stolyarov, V.V. Khmelenko, Low Temp. Phys. 31, 547 (2005)
- 15. S. Mao, R.E. Boltney, V.V. Khmelenko, D.M. Lee, Low Temp. Phys. 38, 1037 (2012)
- A. Meraki, P.T. McColgan, R.E. Boltnev, D.M. Lee, V.V. Khmelenko, J. Low Temp. Phys. 192, 224 (2018)
- 17. S.N. Foner, C.K. Jen, E.L. Cochran, W.A. Bowers, J. Chem. Phys. 28, 351 (1958)
- 18. L.A. Wall, D.W. Brown, R.E. Florin, J. Phys. Chem. 63, 1762 (1959)
- 19. F.J. Adrian, Phys. Rev. **127**, 837 (1962)
- 20. D.D. Delannov, B. Tribollet, F. Valadier, A. Erbeia, J. Chem. Phys. 68, 2252 (1978)
- P.T. McColgan, A. Meraki, R.E. Boltnev, D.M. Lee, V.V. Khmelenko, J. Low Temp. Phys. 187, 124 (2017)



- S. Mao, A. Meraki, P.T. McColgan, V. Shemelin, V.V. Khmelenko, D.M. Lee, Rev. Sci. Instrum. 85, 073906 (2014)
- 23. E.B. Gordon, A.A. Pelmenev, O.F. Pugachev, V.V. Khmelenko, Sov. J. Low Temp. 8(6), 299 (1982)
- 24. E.B. Gordon, L.P. Mezhov-Deglin, O.F. Pugachev, Sov. JETP Lett. 19, 63 (1974)
- 25. E.B. Gordon, L.P. Mezhov-Deglin, O.F. Pugachev, V.V. Khmelenko, Cryogenics 16(9), 555 (1976)
- 26. R. Beringer, M.A. Heald, Phys. Rev. 95, 1474 (1954)
- 27. D.M. Lindsay, J. Chem. Phys 81, 3356 (1984)
- 28. L.B. Knight, J. Steadman J. Chem. Phys **74**(4), 1750–1756 (1982)
- 29. Yu.A. Dmitriev, R.A. Zhitnikov, Zhurnal Tekhnicheskoi Fiziki 57, 1811 (1987)
- 30. C. Kittel, E. Abrahams, Phys. Rev. 90, 238 (1953)
- 31. E.B. Gordon, Low Temp. Phys. 36, 382 (2010)
- 32. A.E. Cuzon, M.J. Eastell, J. Phys. C. 4, 689 (1971)
- 33. R.J. Sayer, R.H. Prince, W.W. Duley, Phys. Stat. Sol. (b) 106, 249 (1981)

Publisher's Note Springer Nature remains neutral with regard to jurisdictional claims in published maps and institutional affiliations.

Springer Nature or its licensor (e.g. a society or other partner) holds exclusive rights to this article under a publishing agreement with the author(s) or other rightsholder(s); author self-archiving of the accepted manuscript version of this article is solely governed by the terms of such publishing agreement and applicable law.

